Genetic and therapeutic heterogeneity shape the baseline and longitudinal immune ecosystem of ovarian clear cell carcinoma

Siyu Xia,[1,2] Lihua Chen,[1,2] Min Yu,[1,2] Jiana Li,[1,2] Jiaxin Chen,[1,2] Fei Xu,[1,2] Mengdong Ni,[1,2] Chaohua Liu,[1,2] Xiaohua Wu (iD),[1,2] Xiaojun Chen,[1,2] Jiajia Li (iD) [1,2]

[1]Department of Gynecologic Oncology, Fudan University Shanghai Cancer Center, Shanghai, Shanghai, China
[2]Department of Oncology, Shanghai Medical College of Fudan University, Shanghai, China

Correspondence to
Dr Jiajia Li;
jiajiali_shca@126.com

Dr Xiaojun Chen;
doccxj2020@163.com

Dr Xiaohua Wu;
wu.xh@fudan.edu.cn

ABSTRACT

Background Ovarian clear cell carcinoma (OCCC) is a rare and chemo-resistant subtype of ovarian cancer. While immunotherapy has demonstrated effectiveness in some OCCC cases, the mechanisms for heterogeneous immunoreactivity and potential combinatory strategies remain unclear.

Methods Tumor samples from 13 patients with OCCC underwent single-cell mRNA-seq and TCR-seq to generate 1 40 683 cells transcriptome, while additionally 31 formalin-fixed paraffin-embedded samples were used for immunohistochemistry. Spatial transcriptomics of two OCCC samples and bulk RNA-seq of 58 patients were incorporated for spatial and interpatient level explorations. Serum tumor markers and radiologic images of three patients with OCCC who received combinatory VEGF and PD-1 inhibition were retrospectively analyzed.

Results OCCC exhibited a dynamic immune architecture shaped by genetic and therapeutic pressure. *ARID1A* mutation linked to baseline immune activation, correlated with an enrichment of neoantigen-reactive CXCL13^{+} CTLA4^{+} CD8^{+} T cells (p<0.001) and enhanced FASLG–FAS interactions. Recurrent OCCC was fibrotic, angiogenic, and immunosuppressive, exhibiting metabolic reprogramming towards activated activity in fatty acid metabolism. High CD36 (log-rank p=0.012, HR: 4.515) and CD47 expression (log-rank p=0.037, HR: 3.246) indicated worse progression-free survival. Treatment with bevacizumab increased intratumoral T cell infiltration and activated T cell interferon-γ signaling. Retrospective analysis of clinical cases revealed that combination therapy with anti-VEGF (vascular endothelial growth factor) and anti-PD-1 agents exerted clinical benefits in patients with OCCC with persistent, recurrent, and metastatic disease.

Conclusions *ARID1A* mutation correlated with OCCC baseline immune activation. Stromal reconstruction and tumor metabolic reprogramming functioned as key processes of OCCC dynamic progression. VEGF inhibition remodeled OCCC stroma, restored T cell function and potentiated immunotherapy. CD36 and CD47 might be potential therapeutic targets for recurrent OCCC.

WHAT IS ALREADY KNOWN ON THIS TOPIC

⇒ Advanced-stage ovarian clear cell carcinoma (OCCC) is chemo-insensitive and associated with unfavorable prognosis. Immunotherapy, especially when combined with other agents, emerges as a novel therapeutic approach for OCCC.

WHAT THIS STUDY ADDS

⇒ *ARID1A* mutation in OCCC linked to baseline immune-activation with enrichment of CXCL13^{+} CTLA4^{+} tumor-reactive T cells. OCCC dynamically manipulated the host environment through tumor-stroma interaction. Upregulation of the tumor metabolic molecules CD36 and CD47, as well as the stromal marker POSTN, were associated with unfavorable clinical outcomes. VEGF inhibition deconstructed tumor stroma and facilitated T cell activation.

HOW THIS STUDY MIGHT AFFECT RESEARCH, PRACTICE OR POLICY

⇒ These findings uncovered a dynamic and multidimensional immune landscape in OCCC, shedding light on the impact of tumor-stroma interplay on recurrence and therapeutic resistance. VEGF inhibition combined with anti-PD1 might be a promising therapeutic strategy for OCCC.

INTRODUCTION

Ovarian cancer (OC) is a highly aggressive gynecologic malignancy, leads to approximately 200 000 women yearly deaths worldwide.[1] Ovarian clear cell carcinoma (OCCC) is relatively rare, accounting for around 10% of OC, which is often diagnosed at an earlier FIGO (International Federation of Gynecology and Obstetrics) stage.[2] However, of all pathologic subtypes, advanced-stage OCCC correlates with the worst prognosis,[3–6] with a 3year overall survival (OS) rate of 53.3% for stage III patients and 29.6% for stage IV patients. Moreover, recurrent OCCCs are platinum-resistant with a less than 10% objective response rate (ORR), underscoring the urgent need for novel therapeutic approaches. Unlike high-grade serous

cancers (HGSCs) that are initiated by *TP53* inactivation and deficiencies in homologous recombination (HR), OCCCs are driven by somatic alterations in PI3K/AKT/mTOR pathway (*PIK3CA* for ~50%) and SWI/SNF chromatin remodeling complex (*ARID1A* for ~50%, *ARID1B* for 6%–18%, *SMARCA4* for 5%–18%).[7] Somatic alterations shape the intratumoral heterogeneity, fuel tumor evolution under extrinsic stresses such as metastatic cloning and chemotherapy, and effected on the tumor microenvironment. Single-cell technology has offered an exceptional opportunity to understand the tumor plasticity and tissue architecture at a higher resolution and comprehensive view,[8–10] paves the way for a deeper understanding of OCCC heterogeneity and mechanisms of therapeutic resistance.

Recent years, immunotherapy emerges as a promising therapeutic avenue for refractory OC, OCCC especially,[11] with several case studies reporting a subset of cases that exhibit strong and sustained responses to immune checkpoint inhibitors (ICIs).[12–14] Epithelial OC showed restrained response to single-agent PD-1/PD-L1 inhibitors, with the ORR primarily ranged around 10%, including PD-1 inhibitors pembrolizumab (8%),[15] nivolumab (7.6%[16]–15%),[17] and PD-L1 inhibitors avelumab (3.7%),[18] BMS-936559 (6.0%),[19] and atezolizumab (22.2%).[20] Although OC might be 'immune-cold' and insensitive to ICIs according to above clinical trials, encouragingly, subgroup analysis implied the potential extraordinary sensitivity of OCCC to PD-1/PD-L1 inhibitors. In phase II KEYNOTE-100 study, patients with OCCC showed a trend toward greater benefits from pembrolizumab (n=19, ORR=15.8%, 95% CI: 3.4% to 39.6%).[15] In phase III study of platinum-resistant OC, patients with OCCC experienced longer OS with nivolumab compared with chemotherapy (gemcitabine or pegylated liposomal doxorubicin) (HR: 0.78; 95% CI: 0.46 to 1.32).[16] Moreover, a transcriptional clear cell signature was significantly higher in complete response (CR) patients with nivolumab treatment.[21] Although larger-scaled clinical trials are still needed to verify above findings, great importance has been attached to clear cell pathology in the ongoing clinical studies on OC immunotherapy.

However, insufficient molecular insights into OCCC immune heterogeneity impeded the development for biomarker discovery and combinatory immunotherapy. While studies in the overall OC population have suggested a series of ICI predictors, including tumor mutational burden,[22] PD-L1 expression, CD8+ T cells infiltration,[15 18] transcriptional signatures of proliferation,[21] glycolysis and hypoxia,[22] and myeloid cell infiltration,[22] little is known about the specific indicators for OCCC immunotherapy. As prevalent genomic events of OCCC, *ARID1A* mutations and deficient mismatch repair have been previously associated with DNA mutability and downstream immune activation.[7 11] Accordingly, a case study reported that patients with OCCC harboring *ARID1A* mutations might be particularly sensitive to immunotherapy.[14] Interestingly, established evidence by immunohistochemistry (IHC) and bulk RNA sequencing have demonstrated the negative clinical correlations of tumor-infiltrating CD8+ T cells, CD4+ T cells, and CD68+ macrophages,[23 24] highlighting the significant immune dysregulation within OCCC. However, little is known about the tissue-specific immunosuppression mechanisms of OCCC, as well as the dynamical processes of how OCCC respond to immunotherapy. It is essential to further explore both the tumor–host interactions specific to OCCC and the detailed functional status of intratumoral immune cells.

Recent years, the application scenarios of single-cell sequencing have been expanded from live tissues to wider-ranged samples including formalin fixed paraffin-embedded (FFPE) blocks.[25] scFFPE-seq provided an opportunity to retrospectively collected clinical samples, thus facilitated investigations of rare diseases, as well as combinatory analysis of corresponding follow-up data. With the advancement in materials availability in single-cell technology, we designed this study with various source of OCCC samples, exploiting both fresh tumors and FFPE samples, to fill in the gap in translational research on OCCC immunobiology.

In the present study, we established a panoramic immune atlas of OCCC at single-cell, spatial and inter-patient dimensions. Analyses of treatment-naïve tumors revealed the impact of *ARID1A* mutation on baseline immune activity. Longitudinal investigations in recurrent tumors demonstrated tumor-stroma interplay as acquired mechanism of immune unresponsiveness. Finally, VEGF inhibition showed the efficacy to reduce stromal density, empower host immunity and might serve as combinatory strategy to facilitate efficient immunotherapy.

METHODS

Human specimen collection

All datasets used in this study are listed in online supplemental table 1. Three in-house datasets involving human subjects were enrolled in this study (dataset 1–3). The study procedures were designed according to the Declaration of Helsinki. Human specimen collection was approved by the ethic committee of Fudan University Shanghai Cancer Center (FUSCC) with the approval number No. 050432-4-2108*. Fresh tumors were collected from five patients with OCCC (dataset 1) during surgery in FUSCC from 2021 to 2023, immersed in DMEM and delivered to the laboratory on ice immediately for tissue dissociation. From 2014 to 2023, tumor samples from 39 patients (dataset 2 and 3) who were pathologically diagnosed with OCCC were collected and preserved as FFPE samples at 4°C. Those patients were followed-up for at least 1 year after surgery, and progression-free survival (PFS) was set as the endpoint of study. Tumor samples from those patients were retrospectively collected and constructed into tumor microarrays for IHC. All patients included in this study approved the utilization of corresponding data and signed written informed consent.

Isolation of cancer-associated fibroblasts (CAFs)

Primary CAFs were isolated from ascites of patients with OC. Briefly, fresh ascites samples were collected from drainage bags, transported on ice and passed through a 70 µm cell strainer to remove large impurities. Subsequently, ascites was centrifuged at 800 rcf for 10 min, and resuspended with DMEM. The red blood cells were removed by Red Blood Cell Lysis Solution (Solarbio), and remaining cells were cultured with Dulbecco's modified eagle medium (DMEM) (without fetal bovine serum). Fibroblasts were separated and purified by differential adhesion method. One hour after cell seeding, the supernatant was collected into a new dish, and adherent cells were gently washed with PBS for three times. Those adherent cells were mainly fibroblasts, cultured with DMEM (10% FBS) at 37°C and were passaged every 4–6 days according to cell density.

CAF co-culture system

Every 3 days, the culturing supernatant of fibroblasts (passage 3–5) was collected and centrifuged at 800 rcf for 3 min to remove cell pellet, adding to the tumor culture dish (supernatant:fresh medium=1:1). Tumor cell lines and cell proliferation assay were described in online supplemental data files.

IMMUNOHISTOCHEMISTRY

The slides were first baked at 65°C for 2 hours. Then, slides were immersed into three washes of dimethylbenzene, and gradient concentration ethanol (SANGON, 100%, 95%, 90%, and 85%) every 10 min in sequence for deparaffinage. Briefly, slides were immersed into antigen retrieval solution (chosen according to the manufactory's instruction) and heated with a pressure cooker for 3 min after boiling. Thereafter, endogenous peroxidase was blocked by 0.3% H_2O_2 for 10 min at room temperature. Incubation of goat serum for 30 min at 37°C was used for nonspecific antigen blocking. Subsequently, slides underwent primary antibody incubation (primary antibodies: anti-rabbit human CD36 antibody, 1:400, proteintech, cat no. 18836-1-AP; anti-mouse human POSTN antibody, 1:4000, proteintech, cat no. 66491-1-Ig; human CD47 IHC kit, cat no. RMA-0842) overnight at 4°C and secondary antibody (proteintech, cat no: RGAR011, RGAM001) incubation at 37°C for 45 min. Coloration of slides by diaminobenzidine (DAB, Solarbio) lasted for 1 min and was terminated by dilated water. For counterstaining, the colored tissue sections were placed into hematoxylin for 2 min. Finally, slides were dehydrated with gradient concentration ethanol (85%, 95%, 100%) every 2 min and underwent xylene transparent for 1–2 min before mounting. Evaluation of IHC was performed by two independent oncologists who were blinded to clinical information. For evaluation of CD36 and CD47, slides with >50% strong staining (brown) tumor area were defined as 'high expression'. For POSTN, slides with >20% strong staining (brown) stromal area were defined as 'high expression'.

WHOLE-EXON SEQUENCING AND IDENTIFICATION OF *ARID1A* MUTATIONS

Genomic DNA from tumor samples was extracted and sequenced by the Illumina NovaSeq platform. GATK4 was used to identify single nucleotide polymorphisms (SNPs) and insertions/deletions (INDELs) within the exon regions and the exon–intron boundary regions. Mutations were annotated with ANNOVAR. Two rounds of quality control were conducted to ensure the validity of mutation recognition. First, SNPs below the following thresholds were filtered out: QD <2.0, MQ <40.0, FS >60.0, SOR >3.0, MQRankSum <−12.5, and ReadPosRankSum <−8.0. Similarly, the INDEL filtering criteria were set at QD <2.0, FS >200.0, SOR >10.0, MQRankSum <−12.5, and ReadPosRankSum <−8.0. Subsequently, mutations with a variant allele frequency (VAF) <5% or mutant allele number <5 or allele sum <20 were filtered out. *ARID1A* mutations were identified according to OncoKB[26] (https://www.oncokb.org/). Patients with *ARID1A* deletions and truncating mutations (loss-of function, and likely pathogenic alterations as suggested as OncoKB) were regarded as *ARID1A* mutant group, other patients who were not detected with those *ARID1A* alterations were classified as *ARID1A* wild-type group (online supplemental table 3).

Single-cell RNA sequencing and scFFPE-seq

Sample preparation, library construction and sequencing were performed according to 10× genomics pipeline. Fresh tumor samples were collected in the DMEM, transported on ice to the laboratory immediately during surgery after sampling. Tumors were minced into pieces as small as possible, and digested with a Tumor Dissociation Kit (Cat. 130-096-730; Miltenyi Biotec) for 30 minutes on a rotator at 37°C. Subsequently, the dissociated cells were passed through a 70 µm cell-strainer (Corning) until single cell suspensions were obtained. The red blood cells were removed by Red Blood Cell Lysis Solution (Solarbio). Single-cell RNA-seq and TCR-seq libraries were prepared using the Chromium Next GEM Single Cell 5′ Kit v2 and Chromium Single Cell Human TCR Amplification Kit from 10× Genomics. FFPE blocks were conducted as 50 µm FFPE curls, and were dissociated with the Miltenyi Biotech FFPE Tissue Dissociation Kit following the manufacturer's instructions and underwent Chromium Fixed RNA Profiling (scFFPE-seq).[25] Above libraries were sent for sequencing based on the Illumina NovaSeq 6000 platform. Single-cell quality control is described in online supplemental data files.

Identification of metaprograms (MPs) by non-negative matrix factorization (NMF) method

MPs of epithelial cells and fibroblasts were identified by the NMF method using GeneNMF package. The merged Seurat object was first split by patient, and consistent NMF MPs were computed across multiple samples with the function 'multiNMF'. NMF MPs were annotated according to program genes and corresponding 'hallmark' and 'GO-BP' pathway activities.

Functional and pathway analysis

Functional pathway activity was analyzed with integrated approaches including AUCell, UCell, and GSVA. Transcriptional factors (TFs) activity of each cell subclusters were predicted by DecoupleR.[27] Copy number alterations of epithelial cells were identified by inferCNV of the Trinity CTAT Project (https://github.com/broadinstitute/inferCNV) with T cells and macrophages as the normal controls. Metabolism[28] framework was used to evaluate metabolic activity of cell clusters.

TRAJECTORY ANALYSIS

Briefly, monocle2,[29] CytoTRACE,[30] and slingshot[31] were used comprehensively to predict the build an evolutionary relationship and trajectory among functional cell subsets. CytoTRACE was used to evaluate cell stemness, the subcluster with the highest CytoTRACE score were presumed at the starting point of developmental route. Monocle2 and slingshot were used to infer the evolutionary trajectory in single-cell-level and subcluster-level, respectively.

Intercellular ligand–receptor interaction analysis

CellChat[32] and NicheNet[33] were used to speculate intercellular interaction within the OCCC tumor microenvironment. Overall interaction number and strength between cell types, as well as focused pathway activity were inferred by CellChat. Nichenet set cell type of interest as the signal receiver and tested how other cells in the tumor microenvironment impact its phenotype. Therefore, we conducted a receiver-focused ligand–receptor analysis with Nichenet to examine how TIME affected effector cells, T cells particularly.

Analysis of spatial transcriptome data

Spatial transcriptomics data were processed by Seurat v4 pipeline. SCT transform was performed and spatial-resolved gene expression was visualized by the function 'SpatialFeaturePlot'. Spots were clustered with the resolution 0.5, and classified into 'Epithelial-rich', 'Stromal-rich', 'Endothelial-rich' and 'Immune-rich' (if presented) regions according to marker genes expression. Cell type signature scores were added to the meta data by UCell method. CellChat V.2 was used for spatial cell–cell communication analysis.

Analysis of bulk RNA sequencing cohorts

Bulk RNA-seq data of OC containing OCCC histologies were deconvoluted by cell type signature scores with ssGSEA methods. Ecotyper[34] was used for immune ecotype prediction.

STATISTICAL ANALYSIS

All graphics and statistical analysis were conducted using Prism V.8.3.0, IBM SPSS V.20 and R V.4.3.2. Detailed packages and computing frameworks are listed in online supplemental table 2. For data fit the normal distribution and homogeneity of variance, parametric tests were priorly chosen. Data that not pass the normality test and homogeneity test of variances were log-transformed or analyzed by non-parametric test as appropriate. All statistical analyses were performed two-sided. $P < 0.05$ was regarded as statistically significant: $*p < 0.05$, $**p < 0.01$, $***p < 0.001$.

DATA AVAILABILITY

All datasets used in this study are listed in online supplemental table 1. The following datasets were obtained from GEO (http://www.ncbi.nlm.nih.gov/geo/): GSE184880[35] (dataset 5); GSE224335[36] (dataset 4); GSE226870[37] (dataset 6). Survival analysis on pan-cancer immunotherapy cohort was performed online using KM-plotter[38 39] (https://kmplot.com/analysis/) (dataset 7). The data generated in this study are available within the article and online supplemental data files. Other data or code are available from the lead contact on reasonable request.

RESULTS

Prospective and retrospective collection of OCCC samples for single-cell profiling

OCCC is relatively rare and poorly differentiated, which poses challenges for fresh sample collection. To provide a comprehensive immune atlas of OCCC, we integrated data from two in-house sequencing cohorts, one prospective and the other retrospective, for single-cell profiling (figure 1A, online supplemental table 1). Detailed clinical information of these patients is shown in online supplemental table 3. The prospective cohort (dataset 1) comprised three recurrent (RC) and two newly diagnosed (ND) fresh tumors obtained during first surgery and confirmed pathologically postsurgery. These samples underwent 5' single-cell RNA-seq and scTCR-seq to generate a high-quality cell type matrix.

The retrospective cohort (dataset 2) comprised eight FIGO stage III OCCC formalin-fixed paraffin-embedded (FFPE) samples, including five ND patients with more than 3 year PFS and three RC patients, for scFFPE-seq analysis. Among the five ND patients, two were identified with somatic *ARID1A* frameshift mutations, while the other two had wildtype *ARID1A*. All three RC cases underwent adjuvant chemotherapy after the initial surgery; two of them received standard TC (Taxol plus Carboplatin) chemotherapy, another one patient received a TC plus VEGFi (bevacizumab) regimen.

For IHC validation, tumor samples from 31 patients with OCCC who underwent surgery at FUSCC between 2014 and 2023 were collected (dataset 3). In addition, one spatial transcriptomics cohort consisting of two patients with OCCC (dataset 4), one external scRNA-seq cohorts of seven HGSC and five normal ovaries (dataset 5), and two bulk RNA-seq datasets (dataset 6 and 7) were obtained for spatial and interpatient level investigations.
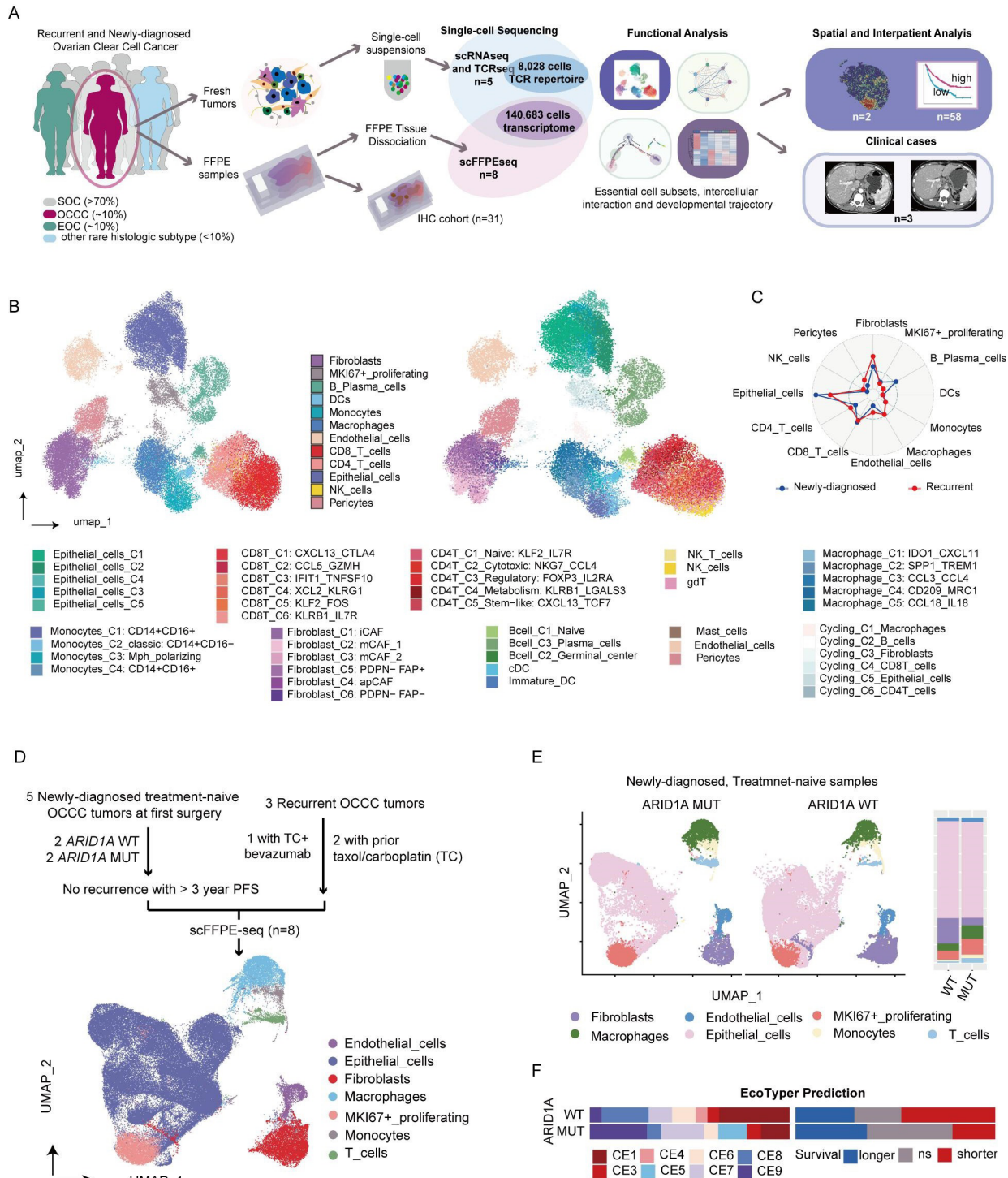
Figure 1 Single-cell multidimensional dissection of OCCC. (A) Study design: five fresh OCCC samples were collected during surgery and underwent single-cell RNA sequencing (scRNA-seq) and single-cell T-cell receptor sequencing (scTCR-seq). Major cell compositions and functional subsets were identified and characterized through integrated analysis. Eight formalin-fixed paraffin-embedded (FFPE) samples with follow-up data were retrospectively collected for scFFPE-seq. Additionally, 31 OCCC samples were used for IHC staining. Analysis on spatial transcriptomics and bulk RNA sequencing datasets were also conducted. (B) Integrative UMAP plot of 49 228 single cell transcriptomics from five harmonized OCCC fresh tumors visualizing main cell compartments (left) and refined cell subsets (right) in OCCC. (C) Radar plot comparing cell proportions in newly diagnosed (blue, n=2) and recurrent OCCC (red, n=3). (D) Flowchart of sample collection for scFFPE-seq and UMAP plot. (E) UMAP plots and bar plot showing the difference in cell composition between ARID1A-mutant (MUT, n=2) and wildtype (WT, n=2) treatment-naive newly diagnosed OCCCs. (F) Bar plot showing the distribution of immune ecotypes and corresponding clinical relevance of ARID1A WT (n=17) and MUT tumors (n=14) in GSE226870 dataset suggested by Ecotyper. FFPE, formalin-fixed paraffin-embedded; IHC, immunohistochemistry; OCCC, ovarian clear cell carcinoma; UMAP, Uniform Manifold Approximation and Projection.

Recurrent OCCC is fibrotic, angiogenic, and immunosuppressive

To construct a high-quality single-cell atlas of OCCC, we first analyzed fresh tumor samples (dataset 1). Following quality control, the remaining 49 228 cells were harmonized to remove batch effects and visualized using the Uniform Manifold Approximation and Projection (UMAP) method (figure 1B). The OCCC ecosystem comprised epithelial, immune, and stromal compartments, which intricately interacted. The cells were categorized into 12 major cell types (online supplemental S1A, B, online supplemental table 4). Additionally, a subset of cells overexpressing proliferation and cell cycle markers were classified as MKI67$^+$ proliferating cells. Compared with newly diagnosed tumors, recurrent OCCC exhibited a fibrotic and angiogenic TIME. All non-immune stroma lineages including fibroblasts, endothelial cells, and pericytes were significantly enriched in recurrent cases (figure 1C). Contrastingly, immune cells were organized heterogeneously, with canonical dendritic cells (cDCs), classic monocytes, M1-polarized macrophages (online supplemental figure S2A, B), and IgM$^+$ plasma cells (online supplemental figure S2C, D) more abundant in newly diagnosed tumors, while M2-polarized macrophages, naive B cells and IgG$^+$ plasma cells accumulated in recurrent tumors.

The major cell types, including epithelial cells, stromal cells, myeloid cells, and T cells, were identifiable in the 91 455 FFPE-based single-cell mixture (dataset 2, figure 1D). To elucidate robust cell–cell interactions within the OCCC microenvironment, we performed CellChat analyses on both fresh tumors (online supplemental S1C) and FFPE samples (online supplemental figure S1D). Consistent findings emerged from both datasets, revealing increased outgoing secreting signaling from fibroblasts, endothelial cells, and macrophages in recurrent tumors, involving networks of periostin, complement, and galectin.

Somatic *ARID1A* mutation correlates with baseline immune activation

Consistent with existing data,[40 41] somatic *ARID1A* mutations were found to be prevalent in our internal OCCC dataset (5/8 in all sequenced patients, online supplemental table 3). When stratifying treatment-naive tumors according to *ARID1A* status (dataset 2), increased T cells and macrophages but decreased fibroblasts were found in *ARID1A* mutant tumors. OCCC with somatic *ARID1A* mutation shaped an immune-enriched and less fibrotic TIME (figure 1E). For broader validation, Ecotyper[34] was employed to deconvolute an OC bulk RNA-seq dataset (dataset 6, GSE226870). A higher proportion of *ARID1A* mutant tumors were classified as carcinoma ecotypes (CE) 8 and CE9, which correlated with longer survival. CE9 was also identified as a biomarker for immunotherapy, prompting further investigation into the immune landscape of *ARID1A* mutant OCCC.

ARID1A mutation also impacted on the cell–cell communication profile (online supplemental figure S1E). Most interestingly, the FASLG–FAS interaction between T cells and malignant cells uniquely detected in *ARID1A* mutant tumors. Surprisingly, the recipient of this signaling was identified as MKI67$^+$ proliferative cells rather than the entire epithelial population, suggesting reduced proliferation as a potential mechanism to evade immune killing. Additionally, T cells in *ARID1A* mutant tumors exhibited activated colony stimulating factor (CSF) signaling that involved in myeloid cells recruitment, offering an explanation for the enrichment of macrophages and macrophage-derived signals.

OCCC epithelial cells are characterized by hypoxia and hypoxic metabolism

To characterize the features and heterogeneity of OCCC epithelial cells, we first focused on cells identified by fresh tumor scRNA-seq (dataset 1). Epithelial cells were observed with vibrant gene copy number variations (CNV) (online supplemental figure S3A), suggesting a malignant status. Consistent with existing experimental studies, transcription factor (TF) analysis revealed *HNF1B*[40] as a key governor of OCCC cells, along with other TFs including *SMARCA4*, *SMARCA1*, *YAP1* and *AR* (online supplemental table 5). To profile the subtype-specific features, pathway activity of epithelial cells from different histologies, including OCCC, HGSC, and normal ovary, was compared using the non-parametric method AUCell (figure 2A). Notably, OCCC cells exhibited heightened activity in hypoxia and hypoxic metabolism pathways including glycolysis, adipogenesis, and fatty acid (FA) metabolism.

To dissect the key biological processes of OCCC, NMF was employed to extract transcriptomic (MPs (figure 2B). Among the 10 identified MPs, only MP2 was associated with cell cycling, while MP5, MP6, and MP9 were linked to epithelial-to-mesenchymal transition (EMT). Additionally, MP1, MP3, MP8, and MP9 indicated cellular hypoxia, and MP3, MP4, and MP9 were correlated with immune activation, again underscoring hypoxia as a central player in OCCC development.

When inquiring how genomic events effect on transcriptional programs, in scFFPE-seq dataset, *ARID1A* mutant tumors showed activated ROS, hypoxia, EMT, cholesterol homeostasis, and adipocyte development pathways (figure 2C). By simulating the evolutionary trajectory, *ARID1A* mutant tumor were positioned on a branch of epithelial cells, demonstrating sustained elevated expression of *ISG15* and *MXRA8* during evolution.

Recurrent tumor cells demonstrate signature of immune evasion and metabolic switch towards FA metabolism

To profile the heterogeneity of epithelial population, five functional subsets were identified from scRNA-seq dataset (figure 2D, online supplemental figure S3B). Cluster 1 (EC1) and cluster 2 (EC2), respectively, represented the majority of ND and RC tumor cells (online supplemental figure S3C). Evolutionary analysis positioned EC2 as a branch of EC1 (figure 2E), with a metabolic transition
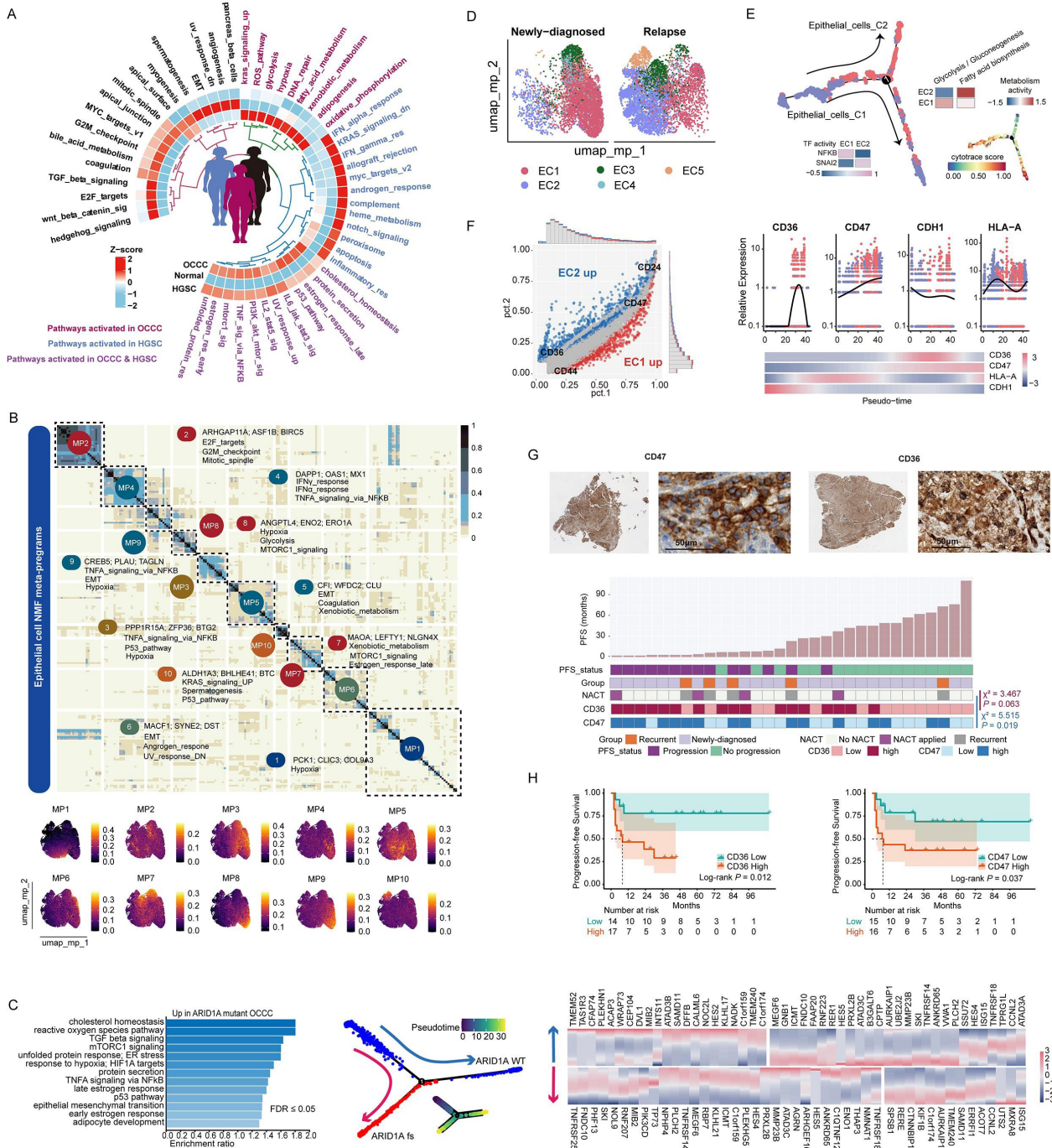
Figure 2 Characteristics and MPs of epithelial cells in OCCC. (A) Heatmap displaying AUCell score of Hallmark pathways across different pathologies (OCCC scRNA-seq cohort: n=5, this article; HGSC scRNA-seq cohort, n=7, GSE184880; normal ovary scRNA-seq cohort, n=5, GSE184880). (B) Heatmap and feature plot showing 10 MPs of OCCC epithelial cells extracted by NMF method. (C) Pathway activity (left), evolutionary trajectory (middle) and trajectory-related gene expression (left) of *ARID1A* MUT OCCC epithelial cells (two patients) compared with *ARID1A* WT cells (two patients) in FFPE cohort. (D) UMAP plot showing five subclusters of 11 448 epithelial cells in OCCC scRNA-seq cohort, and differential distribution in newly diagnosed (n=2) and recurrent OCCC (n=3). (E) Pseudo-time analysis by monocle2 and cell stemness scoring by CytoTRACE in OCCC scRNA-seq cohort uncovered an epithelial cell evolution trajectory from EC1 to EC2. Heatmap showing transcriptional factor and metabolic pathway activity between the two subpopulations. (F) Left: differential gene expression between EC2 and EC1. Right: upregulation of CD36 and CD47 while downregulation of CDH1 and HLA-A throughout the epithelial evolutionary trajectory. (G) Representative IHC staining of CD36 and CD47 in OCCC tumors (left: whole slide, right: high power field, 400×), and correlations (Pearson χ^2 analysis) between CD36 and CD47 expression levels in OCCC IHC cohort (n=31) and presampling NACT. (H) urvival analysis of CD36 and CD47 expression level in OCCC IHC cohort (n=31, outcome: PFS, logrank test). FFPE, formalin-fixed paraffin-embedded; HGSC, high-grade serous cancer; IHC, immunohistochemistry; NACT, neo-adjuvant chemotherapy; NMF, non-negative matrix factorization; OCCC, ovarian clear cell carcinoma; UMAP, Uniform Manifold Approximation and Projection.

from glycolysis to active FA metabolism along the trajectory. Additionally, EC2 exhibited altered gene expression profiles, including decreased HLA-A expression and *NFKB* activity, increased *SNAI2* activity, and loss of E-cadherin expression. By deconvoluting a bulk RNA-seq dataset (online supplemental table 6), we validated that EC1 correlated with immune activation and CD8^{+} T/NK cells infiltration while EC2 was associated with EMT and FA metabolism, at the interpatient level (online supplemental figure S3D, E).

After overlapping trajectory genes identified in fresh sample and FFPE samples, conservative recurrence-related processes were identified, which included FA metabolism and adipocyte development (online supplemental figure S4A, B). Specifically, two FA metabolism-related molecules, CD36 and CD47, were significantly upregulated in EC2 (figure 2F). To investigate the clinical significance of CD36 and CD47, we performed IHC staining on tumor samples from 31 patients with OCCC (dataset 3, figure 2G, online supplemental figure S4C). Interestingly, all patients with prior neoadjuvant chemotherapy showed upregulation of CD36 and CD47 (Pearson χ^2 test p=0.063 and 0.019, respectively). Both CD36 (log-rank p=0.012, HR: 4.515, 95% CI: 1.249 to 16.32) and CD47 abundance (log-rank p=0.037, HR: 3.246, 95% CI: 1.015 to 10.38) correlated worse PFS, indicating their potential linkages with platinum resistance (figure 2H). However, only a borderline statistical significance (Pearson χ^2 p=0.06) was observed regarding the correlation between CD36 expression and platinum-free interval (PFI), while no significant correlation was observed between the CD47 expression level and PFI group (online supplemental table 7), calling on larger-scaled cohort analysis or experimental studies to investigate the roles of FA metabolism pathway in OC platinum resistance.

GeneMANIA analysis showed that SIRPA and THBS1 were key microenvironmental regulators for CD36 and CD47 (online supplemental figure S4D), with myeloid cells and non-immune stromal cells being the major sources of SIRPA and THBS1, respectively (online supplemental figure S4E). Spatial analysis validated the colocalization of those ligand–receptor pairs in OCCC tumor (dataset 4), with CD47-THBS1 being the most prevalent pair, suggestive of the impact of non-immune stromal cells on tumor phenotype.

T cell phenotypes and neoantigen-reactive subsets in OCCC

Intratumoral T cells function as the primary anticancer effectors and are key determinants of immunotherapy sensitivity.[42 43] Our analysis towards the overall OCCC ecosystem indicated comparative CD8^{+} T cells abundance between recurrent tumors and newly diagnosed ones (figure 1C), however, their intercellular communication patterns was altered (online supplemental figure S1C). This phenomenon prompted us to further dissect the functional continuum of CD8^{+} T cells. Therefore, we first classified T cells into CD4^{+}, CD8^{+} and NK cells (figure 3A) and recognized six heterogenous subsets of CD8^{+} T cells

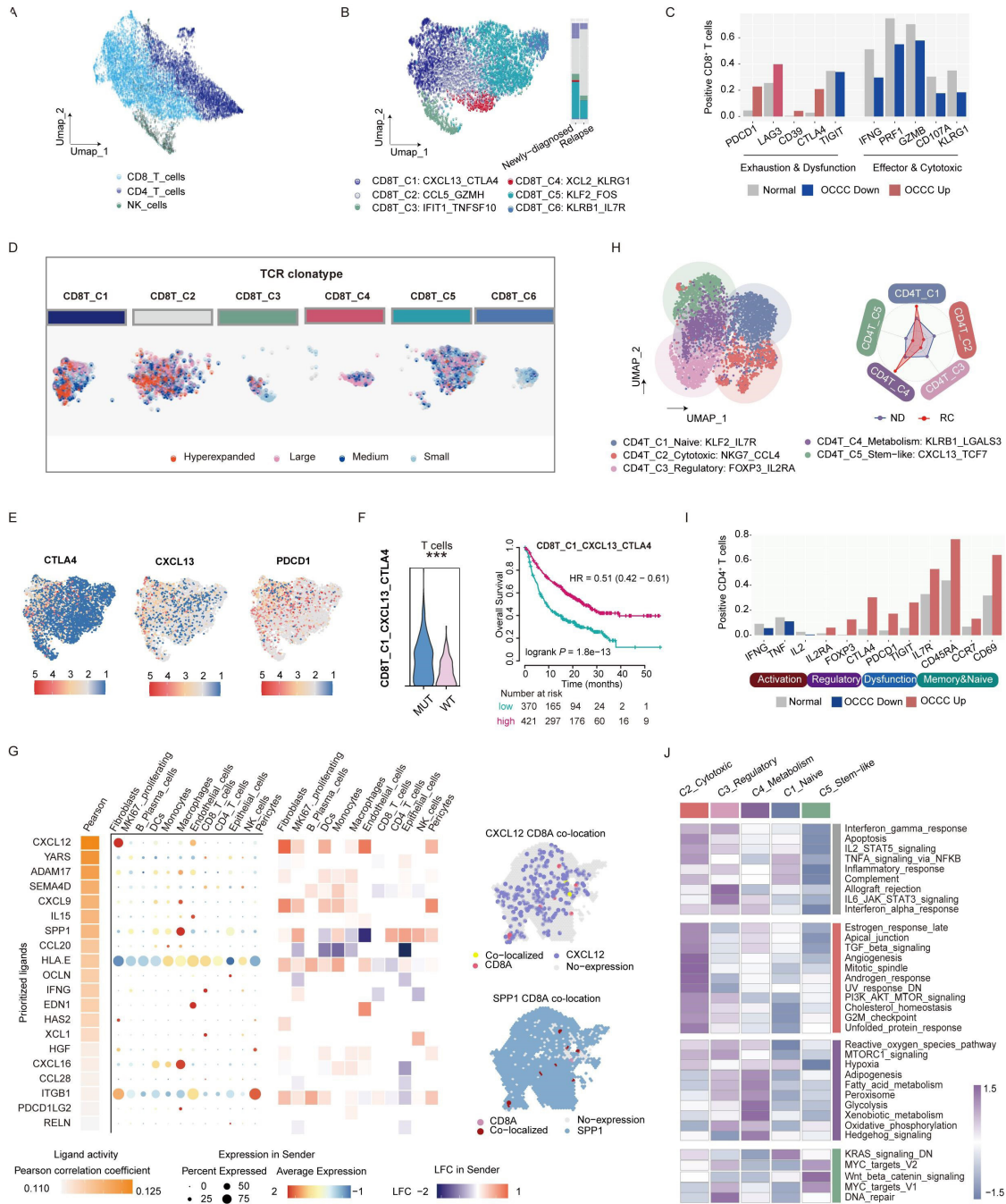within OCCC (figure 3B, online supplemental figure S5A).

Notably, compared with those in normal ovaries, CD8^{+} T cells in OCCC were more exhausted, displayed elevated expression of immune checkpoint markers such as PDCD1, LAG3, CD39, and CTLA4[44], alongside reduced expression of effector molecules including IFNG, GZMB, PRF1, CD107A, and KLRG1 (figure 3C). Two hyperexpanded CD8^{+} T cell subclusters, CXCL13^{+} CTLA4^{+} cluster 1 (enriched in ND), and GZMH^{+} CCL5^{+} cluster 2 (enriched in RC), were potentially neoantigen-responsive based on TCR repertoire analysis (figure 3D). Compared with other subsets, CXCL13^{+} CTLA4^{+} CD8^{+} T subset was terminally differentiated (online supplemental figure S5B), and showed a hyper-activated phenotype with mixed activation and exhaustion markers (F3E, (online supplemental figure S5C, D). Remarkably, T cells in *ARID1A*-mutated OCCCs exhibited higher CXCL13^{+} CTLA4^{+} CD8^{+} T phenotype scores (figure 3F). The presence of CXCL13^{+} CTLA4^{+} CD8^{+} T cells was associated with improved OS in patients receiving immunotherapy (log-rank p<0.001, HR=0.51), suggesting a potentially reversible immune dysregulation state. Ligand–receptor activity analysis uncovered fibroblasts-derived CXCL12 as a key ligand affecting CD8^{+} T cells (figure 3G, online supplemental figure S5E), which was previously linked to immune exclusion[45–47] and tumor metastasis,[48] again highlighting stromal cells as key player in mediating OCCC immunosuppression.

As immunoregulatory subsets, CD4^{+} T cells in OCCC also displayed dysfunctional phenotype, with naive and metabolic subsets accumulated in recurrent tumors (figure 3H–J). Five distinct subclusters were identified within the CD4^{+} T cell population (figure 3H and online supplemental figure S6A–D). Infiltrating CD4^{+} T cells in OCCC displayed reduced production of Th1 cytokines (IFNG, TNF, and IL2), yet elevated expression of regulatory markers (FOXP3 and IL2RA), dysfunctional markers (CTLA4, TIGIT, and PDCD1), and memory-related genes (CCR7, CD69, and CD45RA) (figure 3I). Compared with ND tumors, the diversity of CD4^{+} T cells in recurrent OCCC was found to be constrained. Two subclusters, namely the naive-like C1 (IL7R^{+} KLF2^{+}) and hypermetabolic C4 (KLRB1^{+} LGALS3^{+}), constituted the majority of the CD4^{+} T cell population in recurrent tumors.

Tumor-promoting myofibroblasts are accumulated in recurrent OCCC

Non-immune tumor stroma plays multifaced roles in tumor progression. The current study has indicated the accumulation and enhanced signaling of fibroblasts, pericytes, and endothelial cells during recurrence. We sought to identify the chief culprit throughout the heterogeneous tumor stroma.

Consistent in both fresh tumors and FFPE samples, myofibroblasts (mCAFs) were accumulated in recurrent tumors (figure 4A, B, online supplemental figure S7A–C). A unique subset of chondrocyte-like COLA2^{+} fibroblasts
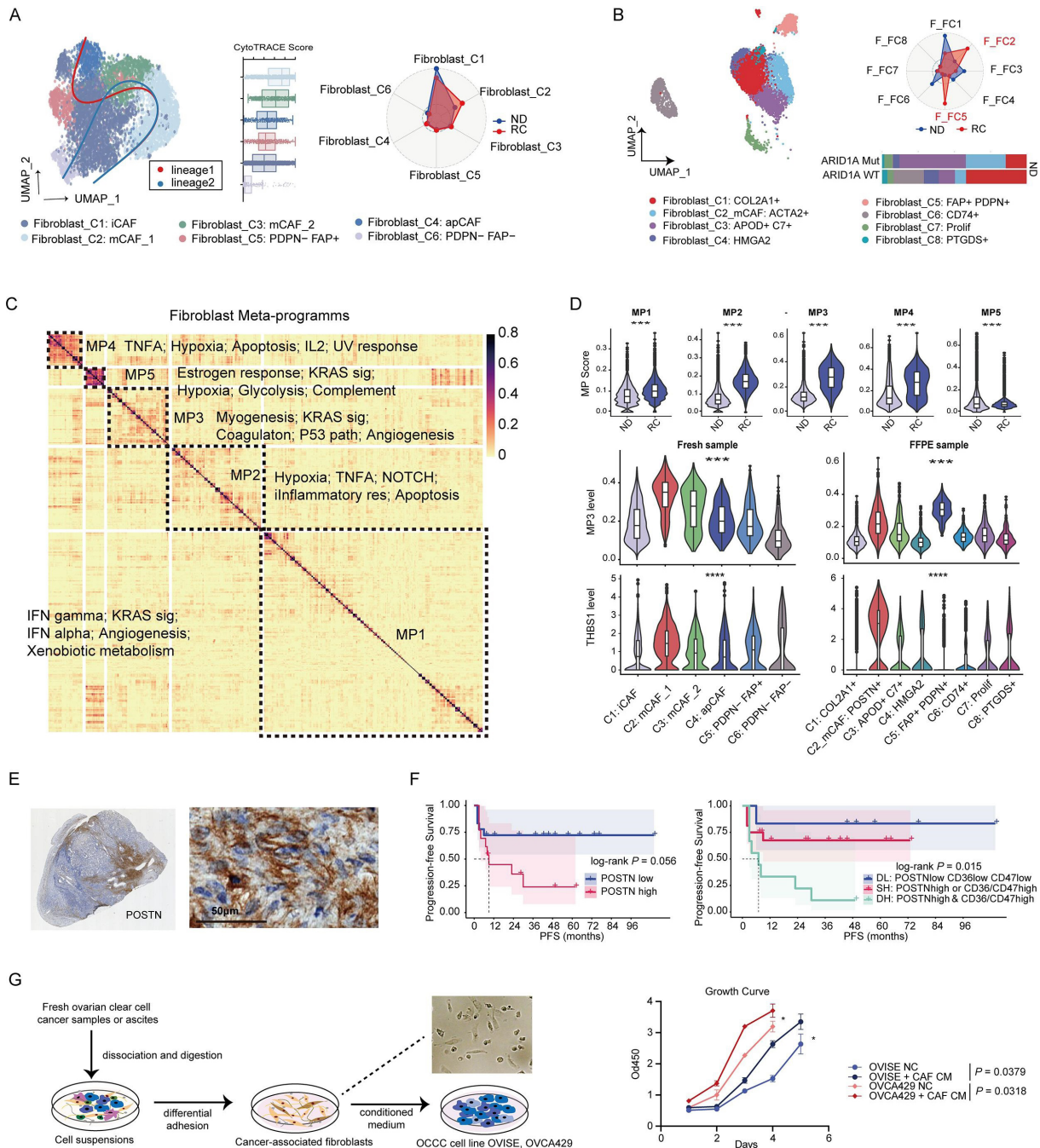
Figure 3 T cell phenotypes and neoantigen-reactive subsets in OCCC. (A) UMAP plot of 12 215 T cells (6554 CD8^{+} T cells, 4746 CD4^{+} T cells, and 915 NK cells) in OCCC scRNA-seq cohort (n=5). (B) Subclustering of CD8^{+} T cells in OCCC scRNA-seq cohort, and differential distribution in newly diagnosed (n=2) and recurrent OCCC (n=3). (C) Comparisons of the proportion of marker gene positive cells of CD8^{+} T cluster between OCCC and normal ovary (OCCC scRNA-seq cohort: n=5, this article; normal ovary scRNA-seq cohort, n=5, GSE184880). (D) Three of the five fresh OCCC tumors (OCCC-3, OCCC-4, OCCC-5) underwent scTCR-seq. Dimplot featuring TCR clonotypes (determined by scRepertoire R package) of CD8^{+} T subclusters. Categories of TCR clonotype were determined by the frequency of a certain TCR clonotype among whole T cell population. Hyperexpanded: beyond 10%; large: 1%–10%; medium: 0.1%–1%; small: 0.001%–0.01%. (E) FeaturePlot marking CTLA4, CXCL13, and PDCD1 expression in CD8^{+} T cells. (F) Left: comparison of CD8_C1_CXCL13_CTLA4 signature UCell score of T cells between *ARID1A* MUT and WT OCCCs (Wilcoxon test). Right: survival curves showing correlation between CD8_C1_CXCL13_CTLA4 signature score and overall survival of pan-cancer patients receiving immunotherapy (log-rank test). (G) Ligand–receptor activity inferred by Nichenet predicted potential regulatory networks of CD8^{+}T cells. (H) Subclustering of CD4^{+} T cells in OCCC scRNA-seq cohort (n=5). (I) Comparisons of essential gene expression frequency in CD4^{+} T cells between OCCC and normal ovary (OCCC scRNA-seq cohort: n=5, this article; normal ovary scRNA-seq cohort, n=5, GSE184880). (J) Hallmark pathway activity of CD4^{+} T cells subclusters in OCCC scRNA-seq cohort (n=5). MUT, mutant; OCCC, ovarian clear cell carcinoma; UMAP, Uniform Manifold Approximation and Projection; WT, wildtype.

Figure 4 Characteristics and MPs of fibroblasts in OCCC. (A) UMAP plot of 7736 fibroblasts identified in OCCC fresh tumors by scRNA-seq (left, n=5). Radar plot showing proportions of fibroblasts subpopulation in newly diagnosed (n=2) and recurrent OCCC (n=3) (right). (B) UMAP plot of fibroblasts in OCCC FFPE samples by scFFPE-seq (left, n=8). Radar plot showing proportions of fibroblasts subpopulation in newly-diagnosed (n=4) and recurrent OCCC (n=4) (right top). Barplot showing proportions of fibroblasts subpopulation in *ARID1A* mutant (n=2) and wildtype (n=2) OCCC. (C) Heatmap showing five MPs of OCCC fibroblasts (n=13) extracted by NMF method. (D) Top: violin plot of MPs activity between fibroblasts from ND and RC tumors (Wilcoxon test, ***p<0.001). Middle and bottom: violin plots of MP3 activity and THBS1 expression level across fibroblasts subsets (Kruskal-Wallis test, ***p<0.001). (E) Representative IHC staining of POSTN in OCCC tumor, left: whole slide, right: high power field, 400×. (F) Survival curves of POSTN expression level in IHC cohort. Outcome: PFS, log-rank test. DL: double low expression of neither tumor marker nor stroma marker (POSTN [low] CD36 [low] CD47 [low]); SH: single high expression of either tumor marker or stroma marker (POSTN [high] CD36 [low] CD47 [low] or POSTN [low] CD36 [high] CD47 [low] or POSTN [low] CD36 [low] CD47 [high]); DH: double high expression of both tumor marker and stroma marker (POSTN [high] CD36 [high] CD47 [high] or POSTN [high] CD36 [high] CD47 [low] or POSTN [high] CD36 [low] CD47 [high]). (G) Scheme of cancer-associated fibroblasts isolation and coculture with tumor cells (left). Growth curve showed that supernatant of fibroblasts culturing medium promoted ovarian tumor proliferation (right, t-test, *p<0.05). FFPE, formalin fixed paraffin-embedded; IHC, immunohistochemistry; MPs, metaprograms; ND, newly diagnosed; OCCC, ovarian clear cell carcinoma; PFS, progression-free survival; RC, recurrent; UMAP, Uniform Manifold Approximation and Projection.

was found only in scFFPE-seq (online supplemental figure S7D). MPs of fibroblasts were identified using the NMF method from integrated scRNA-seq and scFFPE-seq data (figure 4C). MP3, linked to myogenesis and angiogenesis, was increased in recurrent OCCC and associated with mCAFs (figure 4D). Within fibroblast subsets, mCAF_C1 with the most active myogenesis process (online supplemental figure S7E) was located at the origin of the developmental trajectory (figure 4A), presenting as a stem-like recurrence-related subset. This subset was controlled by TGF-β signaling-related TFs including *MYOCD*, *SRF*, and *SMAD1* (online supplemental figure S7F) and showed activated lipid metabolism (online supplemental figure S7G). Interestingly, mCAFs, especially the POSTN$^+$ subset, were the main source of THBS1 (figure 4D), and therefore might be key regulators of tumor phenotype.

We conducted IHC staining of POSTN in OCCC tissues (figure 4E). Denser POSTN expression was observed in recurrent OCCC compared with newly diagnosed tumors (online supplemental figure S7H). High POSTN expression alone showed a borderline significant correlation with unfavorable PFS (log-rank p=0.056). However, when tumor CD36/CD47 levels were included in the analysis, patients with tumors that were double positive for CD36 or CD47 and stroma POSTN exhibited the significantly worst PFS (log-rank p=0.015) (figure 4F). Additionally, the addition of culture supernatant from cancer-associated fibroblasts isolated from surgical samples (online supplemental figure S7I) to an OCCC cell line culture system promoted tumor cell growth (figure 4G) and induced CD36 expression (online supplemental figure S7J).

Endothelial cells and pericytes form a vascular niche and correlate with unfavorable immune ecotype

Pericytes and endothelial cells are main components of tumor vascular structure. To visualize the spatial colocation of those cells in OCCC, UCell method was used to annotate each spot in spatial transcriptomic data (figure 5A and online supplemental figure S8A). The 'Endothelial-rich' regions showed typically codistribution of endothelial cells and pericytes, representing the vascular structure within OCCC tumors, consistent with histologic findings. Naive CD4$^+$ T cells were primarily located around the vessels rather than in the tumor core, which partially explains their lack of expression of immune activation or regulatory molecules. The tumor stroma trapped a group of immunosuppressive cell subsets, including M2-polarized macrophages and metabolic CD4$^+$ T cells. In contrast, tumor cores showed minimal immune infiltration. Additionally, the chemosensitive OCCC formed an immune-reactive interface characterized by an enrichment of DCs, M1-polarized macrophages, monocytes, apCAFs, and cluster 1 epithelial cells (online supplemental figure S8A).

Interpatient level analysis revealed the associations between cell subsets and ecosystem construction. Intriguingly, patients with OCCC with infiltrated TIME were classified into two distinct ecotypes, EC1 and EC9, which

showed reverse clinical associations (online supplemental figure S8B). The most significant difference between the two subsets was the abundance of stromal cells. Among all cell subsets, B lineage was the only one that predicted a favorable carcinoma ecotype (online supplemental figure S8C, top; AUC: 0.709, p=0.011). On the contrary, pericytes (AUC: 0.101, p<0.001), mCAFs (AUC: 0.201, p<0.001), and endothelial cells (AUC: 0.283, p=0.008) were negative predictors of a good CE type.

VEGF inhibition remodels the tumor stroma and reinvigorates tumor-infiltrating T cells

Given the association with the immunosuppressive ecotype of the vascular structure, we investigated whether VEGF inhibition could improve the TIME. Comparing patients who received merely TC (Taxol plus Carboplatin) chemotherapy with those who received combinatory TC plus bevacizumab, we found that the application of bevacizumab increased the proportion of intratumoral T cells while reducing the abundance of fibroblasts (figure 5B). T cells in VEGFi-treated tumors displayed higher scores for CD8 cytotoxicity, CD8 IFN response, CD4 activation effector function, CD4 IFN response, but lower levels of CD4 naïve score,[39] indicating an immune activated status (figure 5C). Cell–cell communication patterns were also altered in VEGFi-treated OCCC (figure 5D). Fibroblast-derived POSTN and SEMA3 signaling were reduced in VEGFi-treated OCCC, while CCL and galectin networks were upregulated. The patterns of VEGF signaling differed between tumors treated with TC and TC plus VEGFi. Upregulated VEGF signaling from myeloid cells and epithelial cells in VEGFi-treated OCCC partially accounted for the recurrence after adjuvant therapy.

VEGFi plus anti-PD-1 exerts clinical benefit in refractory OCCC

To evaluate the efficacy of VEGFi plus anti-PD1 in OCCC in a clinical and real-world context, we conducted a retrospective analysis of clinical cases. Clinical benefits from VEGFi plus PD1 inhibition were observed in persistent (figure 6A), recurrent (figure 6B), and metastatic (figure 6C) patients with OCCC, either combined with adjuvant chemotherapy or as maintenance treatment.

Case 1 involved a patient with *ARID1A* mutant OCCC with persistent disease after 2 cycles of TC adjuvant chemotherapy. The patient's serum CA125 levels returned to the normal range after adding VEGFi plus anti-PD1 to the chemotherapy regimen (from 154 U/mL to 11.5 U/mL), and achieved radiologic partial remission (figure 6A). Case 2 was a patient with *ARID1A* wildtype OCCC who experienced platinum-resistant recurrence. The patient's tumor markers remained within normal limits until 9 months after the first surgery (figure 6B). PET-CT indicated new lesions of retroperitoneal lymph node metastasis. While TC plus VEGFi treatment failed to control the elevated serum CA199, the application of GP (gemcitabine+cisplatin) + VEGFi + anti-PD1 combinatory treatment resulted in partial remission. Case 3 involved a patient with *ARID1A* wildtype stage IV OCCC with liver
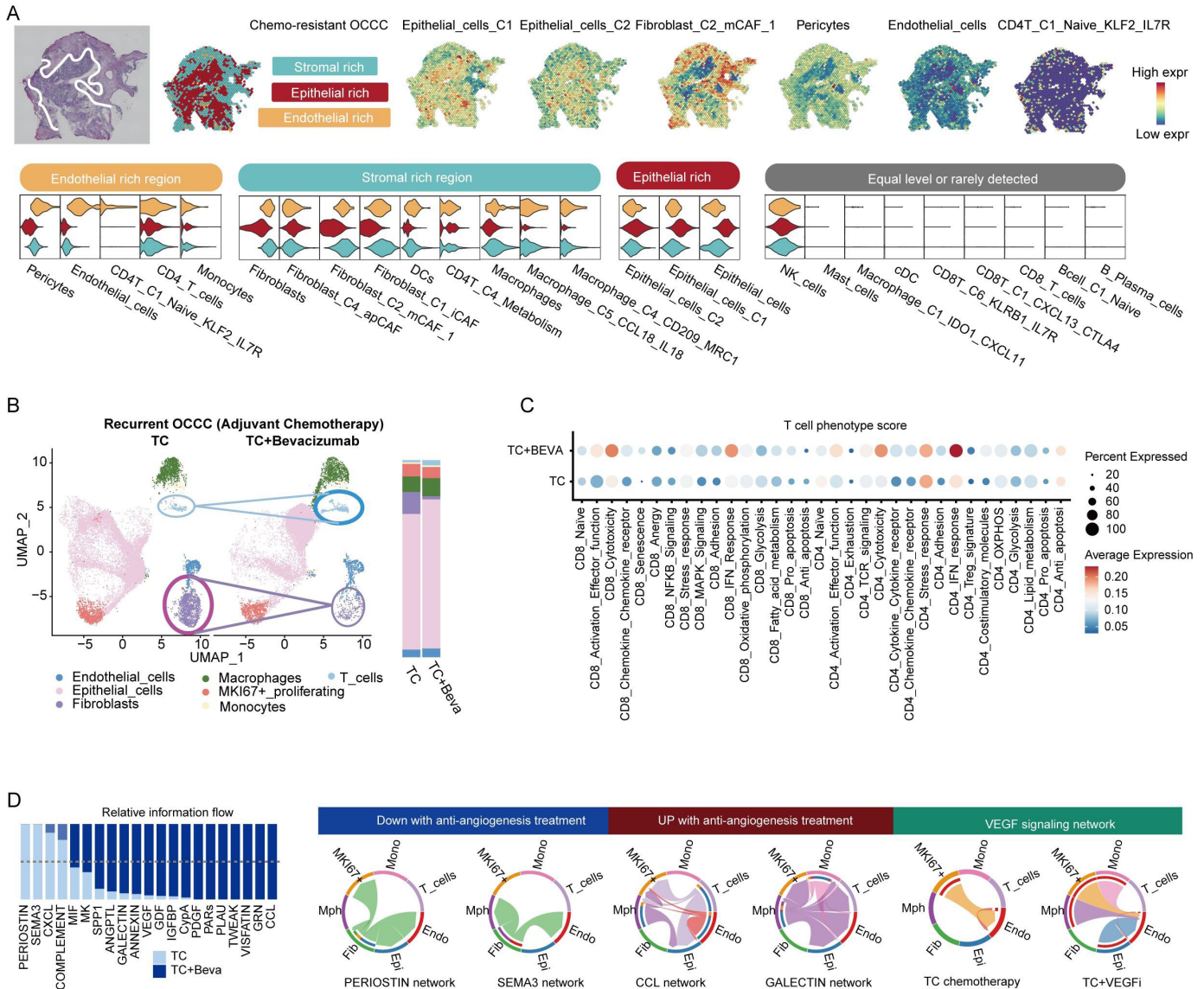
Figure 5 VEGF inhibition reinvigorates T cell function. (A) Spatial characterization of OCCC sample. Feature plots and violin plots showing distribution of lineage signature score (calculated by UCell method) in different niches (epithelial-rich, stromal-rich, endothelial-rich and immune-rich). (B) UMAP plot and bar plot showing cell composition of recurrent OCCC with or without adjuvant bevacizumab treatment. (C) Dot plot of T cell phenotype score between patients receiving TC (Taxol plus carboplatin) chemotherapy and TC+BEVA (bevacizumab) adjuvant regimen. (D) Barplot of relative cell-cell communication network activity between TC and TC+BEVA subgroup patients with OCCC. OCCC, ovarian clear cell carcinoma; UMAP, Uniform Manifold Approximation and Projection.

metastasis. The patient's serum CA125 levels decreased from 227 U/mL to 27.1 U/mL after two cycles of DO (docetaxel+oxaliplatin) chemotherapy plus VEGFi and anti-PD-1 (figure 6C). While well-designed prospective clinical trials are still needed to accurately assess the rate of clinical benefit of this combinatory therapy in OCCC, the cases discussed above provide preliminary evidence of the efficacy of VEGFi plus anti-PD-1 in refractory OCCC, irrespective of *ARID1A* status and disease course (figure 6D).

DISCUSSION

Advanced-stage OCCCs present a significant challenge due to their high malignancy and resistance to chemotherapy. To facilitate development of OCCC immunotherapy, we collected OCCC samples from all available sources, including fresh tumors and FFPE samples, and used single-cell technologies to establish a multidimensional and dynamic immune atlas of OCCC. OCCC exhibits distinct genomic features, with approximately 50% of cases harboring somatic *ARID1A* mutations.[49] Consistent with previous studies in other malignancies,[50] *ARID1A* mutation in OCCC linked to baseline immune activation and pre-existing tumor-reactive T cells.
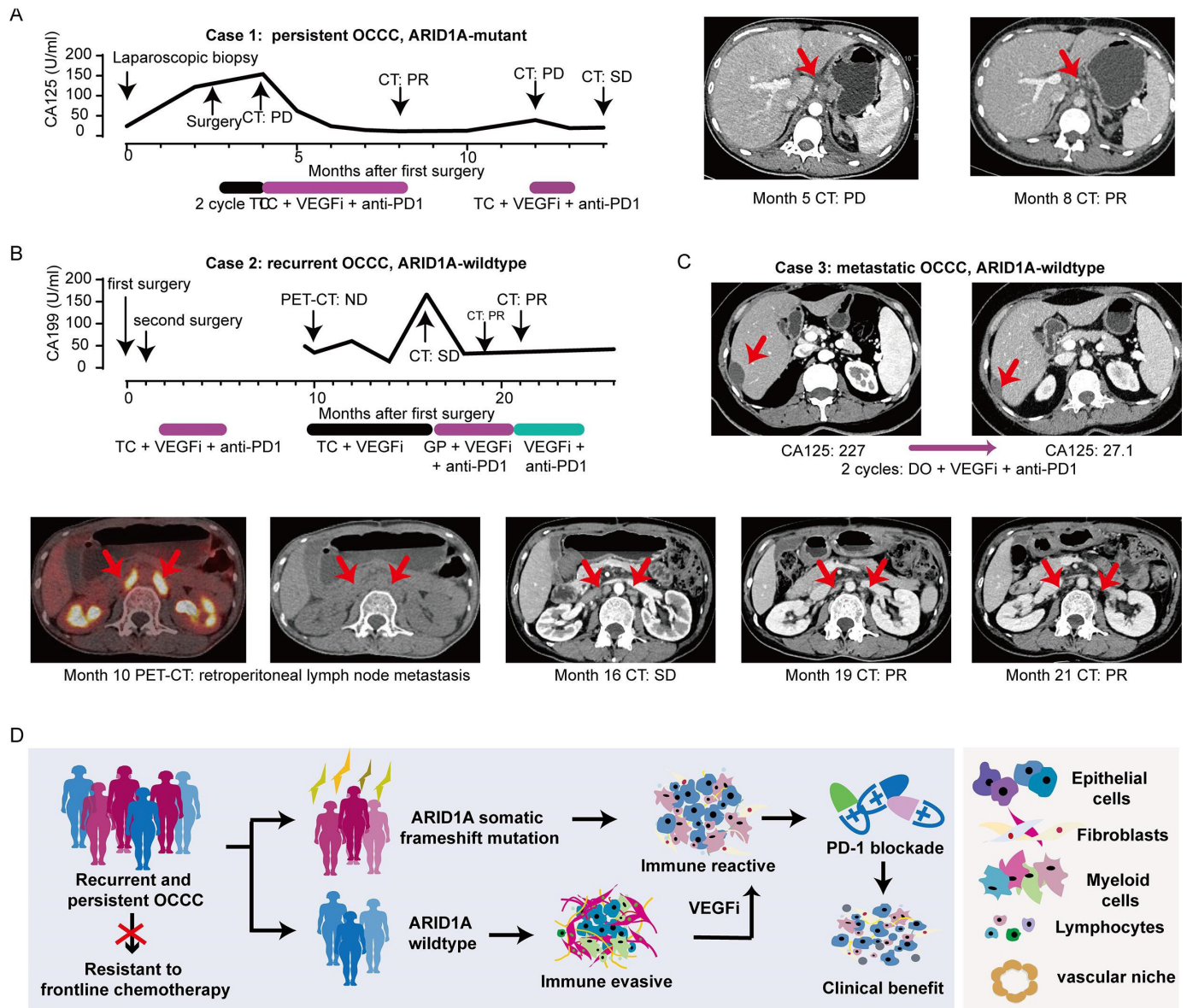
Figure 6 VEGFi plus anti-PD-1 exerts clinical benefit in refractory OCCC. (A) Line chart showing dynamic changes of cancer antigens of persistent OCCC case 1 and representative CT images who received VEGF inhibition plus anti-PD1 during the course of disease. (B) Line chart showing dynamic changes of cancer antigens of recurrent OCCC case 2 and representative PET-CT and CT images who received VEGF inhibition plus anti-PD1 during the course of disease. (C) OCCC case 3: metastatic patients with OCCC received anti-PD1/CTLA4 treatment. (D) Graphical abstract. OCCC, ovarian clear cell carcinoma.

Growing clinical trials are carrying out to systemically assess the efficacy of ICIs in OCCC, especially in combination with front-line pharmaceuticals and other immunomodulatory agents. For combinatory PD-1/CTLA4 blockade, nivolumab plus ipilimumab achieved an approximately threefold ORR (31.4%, 16/51) than nivolumab monotherapy, with clear cell histology more likely (logistic regression OR: 5.205) to respond when compared with other histologic subtypes.[51] Combination therapy with novel immunomodulatory agents including IDO1 inhibitor epacadostat (ORR: 21.4%)[52] are also evaluated. Interestingly, PD-1/PD-L1 blockade plus anti-angiogenic agents exerted noticeable clinical effects. Pembrolizumab in combination with bevacizumab achieved 28.9% ORR[53] in recurrent OC, and 47.5% when combined with oral metronomic cyclophosphamide.[54] In a phase I study of the anti-PD-1/VEGFA bispecific antibody AK112, two out of three patients with platinum-resistant OCCC achieved a partial response (ORR: 66.7%).[55] This ORR exceeded the average level in both patients with OC (5/19, ORR: 26.3%) and the entire solid tumor cohort (12/47, ORR: 25.5%). Emerging clinical trials are designed to test various ICI-based therapeutic combinations in recurrent and refractory OCCC. Those combinations mainly focused on the combination of PD-1/PD-L1 inhibitors and antiangiogenic drugs including Anlotinib (NCT05600998), Sintilimab (NCT04735861), Lenvatinib (NCT05296512), and AK112 (NCT06560112). To expand the therapeutic arsenal of OCCC, efforts are also made in investigating ICIs in combination with novel inhibitors,

including BRCA1/2 inhibitor Pamiparib (NCT05044871), TIGIT inhibitor Etigilimab (NCT05715216), PP2A inhibitor LB-100 (NCT06065462), and HER2 ADC drug Disitamab vedotin (RC48) (NCT06540729). Particularly, one study brings AK104 (PD-1/CTLA-4 bispecific) plus chemotherapy into the context of neoadjuvant treatment (NCT06542549). Another study examining the combination of ATR inhibitor AZD6738, Olaparib and durvalumab takes *ARID1A* mutation into study design (NCT04065269). In the following decade, results from these trials will provide clinical-level evidences to facilitate individualized ICI-based therapies for patients with OCCC with diverse molecular events.

In this context, a major translational significance gained by our study is to biologically explain why patients with OCCC might benefit from anti-PD-1 plus VEGFi. During recurrence, OCCC tumor cells orchestrated an immunosuppressive microenvironment through dynamic reconstruction of the tumor stroma. Spatial analysis showed that the colocalization of endothelial cells and RGS5+ pericytes[56] formed a typical vascular region in OCCC. Tumor cores in recurrent OCCC displayed minimal immune cell infiltration, in contrast to higher concentrations of immune cells in the stromal and perivascular regions. VEGF inhibition led to decreased stroma density, increased T cell infiltration, and reactivation of T cells towards IFNγ signaling and cytotoxicity. To obtain real-world level evidences, we reviewed a series of clinical cases. Combining VEGFi with anti-PD-1 in OCCC resulted in both biochemical and radiological response in patients with OCCC with persistent, recurrent, and metastatic disease, regardless of *ARID1A* status, thereby expanding the treatment options for OCCC.

Besides using VEGF inhibition to sensitize OCCC immunotherapy, our data also pinpointed new avenues for OCCC therapeutics. The longitudinal analysis of OCCC immune contexture provided an evolutionary perspective of how OCCC dynamically manipulated the host environment to evade immune killing. Recurrent tumor cells showed downregulation of HLA class I molecule but upregulation of the anti-phagocytosis receptor CD47. Antigen-presenting cells including classic DCs and IDO1+ CXCL10+ M1-polarized macrophages were dramatically reduced within recurrent tumors. Contrastingly, the non-immune stromal compartments consisted by fibroblasts, endothelial cells and pericytes were enriched in recurrent tumors and showed enhanced intercellular regulatory potential. The myofibroblast emerged as a central player in OCCC, exerting influence on both tumor phenotype through the CD47/THBS1 axis and T cell function through the CXCL12/CXCR4 pathway. These findings placed strategies to target stroma cells as future directions for OCCC treatment.

Our data also highlighted metabolic reprogramming[57] as a targetable hallmark of OCCC. OCCC tumors displayed higher hypoxic metabolic activity compared with serous tumors, with recurrent OCCC tumors showing a shift from glycolysis to FA metabolism, marked by increased CD47

and CD36 expression. Additionally, CD4+ T cell in recurrent OCCC showed restricted diversity, with two main clusters representing naive and hypermetabolic states, suggesting reduced functionality due to microenvironmental hypoxia. Accordingly, a previous study suggested hypoxia transcriptional signature negatively correlated with clinical outcomes of patients with OC who received anti-PD-1 treatment.[22] Whether targeting FA metabolism with statins or other novel agents could reverse chemoresistance demands further investigations, as several clinical trials are ongoing regarding the use of statins in OC (NCT06468254, NCT06468254, NCT03532139).

Finally, scFFPE-seq has revolutionized the landscape of single cell technology, and may promote the research of rare diseases. While existing studies have inferred the consistency between fresh cell scRNA-seq and scFFPE-seq using short-term preserved samples (<1 year), they also raise questions about how scFFPE performs with older FFPE blocks after years of preservation.[58] Our data indicated that scFFPE-seq was capable of depicting both the cell composition and functional phenotype using FFPE blocks preserved for 2–7 years, enabling the use of scFFPE-seq to analyze samples with long-term follow-up data. Notably, scFFPE-seq was more efficient in capturing epithelial cells and fibroblasts, and uncovered a novel subset of type II collagen secreting fibroblasts.

Certain limitations were presented in the current study. First, our general sample size is relatively small. Although we have employed various analytical methodologies and external datasets to enhance the validity and robustness of our findings, we were unable to achieve statistical significance in certain aspects of the analysis. Further research in larger patient with OCCC population is essential to deepen our understanding of the immune microenvironment in OCCC. Additionally, this study was primarily computational and correlational, leaving several biological assumptions to be experimentally and interventionally validated. Given the current lack of efficient disease models for OCCC research, the establishment of cancer models, particularly immune-competent patient-derived organoids or xenografts, could be crucial.

Taken together, this study provided a single-cell immune atlas of OCCC, assessing clinical and genomic factors in influencing OCCC immune contexture and tracing the dynamics during tumor recurrence. Although OCCC acquired chemoresistance and immunosuppression through metabolic reprogramming and stromal remodeling, VEGF inhibition reactivated anti-tumor immunity and potentiated immunotherapy.

ORCID iDs
Xiaohua Wu http://orcid.org/0000-0002-2271-2514
Jiajia Li http://orcid.org/0009-0002-2792-0803

REFERENCES

1 Sung H, Ferlay J, Siegel RL, et al. Global Cancer Statistics 2020: GLOBOCAN Estimates of Incidence and Mortality Worldwide for 36 Cancers in 185 Countries. CA Cancer J Clin 2021;71:209–49.
2 Shu CA, Zhou Q, Jotwani AR, et al. Ovarian clear cell carcinoma, outcomes by stage: the MSK experience. Gynecol Oncol 2015;139:236–41.
3 Itamochi H, Kigawa J, Terakawa N. Mechanisms of chemoresistance and poor prognosis in ovarian clear cell carcinoma. Cancer Sci 2008;99:653–8.
4 Anglesio MS, Carey MS, Köbel M, et al. Clear cell carcinoma of the ovary: A report from the first Ovarian Clear Cell Symposium, June 24th, 2010. Gynecol Oncol 2011;121:407–15.
5 Lee Y-Y, Kim T-J, Kim M-J, et al. Prognosis of ovarian clear cell carcinoma compared to other histological subtypes: a meta-analysis. Gynecol Oncol 2011;122:541–7.
6 Chan JK, Teoh D, Hu JM, et al. Do clear cell ovarian carcinomas have poorer prognosis compared to other epithelial cell types? A study of 1411 clear cell ovarian cancers. Gynecol Oncol 2008;109:370–6.
7 Khalique S, Lord CJ, Banerjee S, et al. Translational genomics of ovarian clear cell carcinoma. Semin Cancer Biol 2020;61:121–31.
8 Han G, Sinjab A, Rahal Z, et al. An atlas of epithelial cell states and plasticity in lung adenocarcinoma. Nature New Biol 2024;627:656–63.
9 Gavish A, Tyler M, Greenwald AC, et al. Hallmarks of transcriptional intratumour heterogeneity across a thousand tumours. Nature New Biol 2023;618:598–606.
10 Izar B, Tirosh I, Stover EH, et al. A single-cell landscape of high-grade serous ovarian cancer. Nat Med 2020;26:1271–9.
11 Ghisoni E, Morotti M, Sarivalasis A, et al. Immunotherapy for ovarian cancer: towards a tailored immunophenotype-based approach. Nat Rev Clin Oncol 2024;21:801–17.
12 Calo CA, Levine MD, Brown MD, et al. Combination lenvatinib plus pembrolizumab in the treatment of ovarian clear cell carcinoma: A case series. Gynecol Oncol Rep 2023;46:101171.
13 Sia TY, Manning-Geist B, Gordhandas S, et al. Treatment of ovarian clear cell carcinoma with immune checkpoint blockade: a case series. Int J Gynecol Cancer 2022;32:1017–24.
14 Lin Y-C, Wen K-C, Sung P-L, et al. Complete remission of heavily treated ovarian clear cell carcinoma with ARID1A mutations after pembrolizumab and bevacizumab combination therapy: a case report. J Ovarian Res 2020;13:143.
15 Matulonis UA, Shapira-Frommer R, Santin AD, et al. Antitumor activity and safety of pembrolizumab in patients with advanced recurrent ovarian cancer: results from the phase II KEYNOTE-100 study. Ann Oncol 2019;30:1080–7.
16 Hamanishi J, Takeshima N, Katsumata N, et al. Nivolumab Versus Gemcitabine or Pegylated Liposomal Doxorubicin for Patients With Platinum-Resistant Ovarian Cancer: Open-Label, Randomized Trial in Japan (NINJA). JCO 2021;39:3671–81.
17 Hamanishi J, Mandai M, Ikeda T, et al. Safety and Antitumor Activity of Anti-PD-1 Antibody, Nivolumab, in Patients With Platinum-Resistant Ovarian Cancer. J Clin Oncol 2015;33:4015–22.
18 Pujade-Lauraine E, Fujiwara K, Ledermann JA, et al. Avelumab alone or in combination with chemotherapy versus chemotherapy alone in platinum-resistant or platinum-refractory ovarian cancer (JAVELIN Ovarian 200): an open-label, three-arm, randomised, phase 3 study. Lancet Oncol 2021;22:1034–46.
19 Brahmer JR, Tykodi SS, Chow LQM, et al. Safety and Activity of Anti–PD-L1 Antibody in Patients with Advanced Cancer. N Engl J Med 2012;366:2455–65.
20 Liu JF, Gordon M, Veneris J, et al. Safety, clinical activity and biomarker assessments of atezolizumab from a Phase I study in advanced/recurrent ovarian and uterine cancers. Gynecol Oncol 2019;154:314–22.
21 Murakami R, Hamanishi J, Brown JB, et al. Combination of gene set signatures correlates with response to nivolumab in platinum-resistant ovarian cancer. Sci Rep 2021;11:11427.
22 Ledermann JA, Shapira-Frommer R, Santin AD, et al. Molecular determinants of clinical outcomes of pembrolizumab in recurrent ovarian cancer: Exploratory analysis of KEYNOTE-100. Gynecol Oncol 2023;178:119–29.
23 Devlin M-J, Miller R, Laforets F, et al. The Tumor Microenvironment of Clear-Cell Ovarian Cancer. Cancer Immunol Res 2022;10:1326–39.
24 Sue-A-Quan R, Patel PG, Shakfa N, et al. Prognostic significance of T cells, PD-L1 immune checkpoint and tumour associated macrophages in clear cell carcinoma of the ovary. Gynecol Oncol 2021;162:421–30.
25 Janesick A, Shelansky R, Gottscho AD, et al. High resolution mapping of the breast cancer tumor microenvironment using integrated single cell, spatial and in situ analysis of ffpe tissue. Cancer Biology [Preprint] 2022.
26 Suehnholz SP, Nissan MH, Zhang H, et al. Quantifying the Expanding Landscape of Clinical Actionability for Patients with Cancer. Cancer Discov 2024;14:49–65.
27 Badia-i-Mompel P, Vélez Santiago J, Braunger J, et al. decoupleR: ensemble of computational methods to infer biological activities from omics data. Bioinf Adv 2022;2:vbac016.
28 Wu Y, Yang S, Ma J, et al. Spatiotemporal Immune Landscape of Colorectal Cancer Liver Metastasis at Single-Cell Level. Cancer Discov 2022;12:134–53.
29 Trapnell C, Cacchiarelli D, Grimsby J, et al. The dynamics and regulators of cell fate decisions are revealed by pseudotemporal ordering of single cells. Nat Biotechnol 2014;32:381–6.
30 Gulati GS, Sikandar SS, Wesche DJ, et al. Single-cell transcriptional diversity is a hallmark of developmental potential. Science 2020;367:405–11.
31 Street K, Risso D, Fletcher RB, et al. Slingshot: cell lineage and pseudotime inference for single-cell transcriptomics. BMC Genomics 2018;19:477.
32 Jin S, Guerrero-Juarez CF, Zhang L, et al. Inference and analysis of cell-cell communication using CellChat. Nat Commun 2021;12:1088.
33 Browaeys R, Saelens W, Saeys Y. NicheNet: modeling intercellular communication by linking ligands to target genes. Nat Methods 2020;17:159–62.
34 Luca BA, Steen CB, Matusiak M, et al. Atlas of clinically distinct cell states and ecosystems across human solid tumors. Cell 2021;184:5482–96.
35 Xu J, Fang Y, Chen K, et al. Single-Cell RNA Sequencing Reveals the Tissue Architecture in Human High-Grade Serous Ovarian Cancer. Clin Cancer Res 2022;28:3590–602.
36 Mori Y, Okimoto Y, Sakai H, et al. Targeting PDGF signaling of cancer-associated fibroblasts blocks feedback activation of HIF-1alpha and tumor progression of clear cell ovarian cancer. Cell Rep Med 2024;5:101532.

37 Beddows I, Fan H, Heinze K, *et al*. Cell State of Origin Impacts Development of Distinct Endometriosis-Related Ovarian Carcinoma Histotypes. *Cancer Res* 2024;84:26–38.

38 Gyorffy B. Discovery and ranking of the most robust prognostic biomarkers in serous ovarian cancer. *Geroscience* 2023;45:1889–98.

39 Kovacs SA, Fekete JT, Gyorffy B. Predictive biomarkers of immunotherapy response with pharmacological applications in solid tumors. *Acta Pharmacol Sin* 2023;44:1879–89.

40 Iida Y, Okamoto A, Hollis RL, *et al*. Clear cell carcinoma of the ovary: a clinical and molecular perspective. *Int J Gynecol Cancer* 2021;31:605–16.

41 Takahashi K, Takenaka M, Kawabata A, *et al*. Rethinking of treatment strategies and clinical management in ovarian clear cell carcinoma. *Int J Clin Oncol* 2020;25:425–31.

42 Fridman WH, Zitvogel L, Sautès-Fridman C, *et al*. The immune contexture in cancer prognosis and treatment. *Nat Rev Clin Oncol* 2017;14:717–34.

43 Chu Y, Dai E, Li Y, *et al*. Pan-cancer T cell atlas links a cellular stress response state to immunotherapy resistance. *Nat Med* 2023;29:1550–62.

44 Chow A, Perica K, Klebanoff CA, *et al*. Clinical implications of T cell exhaustion for cancer immunotherapy. *Nat Rev Clin Oncol* 2022;19:775–90.

45 Garg B, Giri B, Modi S, *et al*. NFκB in Pancreatic Stellate Cells Reduces Infiltration of Tumors by Cytotoxic T Cells and Killing of Cancer Cells, via Up-regulation of CXCL12. *Gastroenterology* 2018;155:880–91.

46 Zboralski D, Hoehlig K, Eulberg D, *et al*. Increasing Tumor-Infiltrating T Cells through Inhibition of CXCL12 with NOX-A12 Synergizes with PD-1 Blockade. *Cancer Immunol Res* 2017;5:950–6.

47 Feig C, Jones JO, Kraman M, *et al*. Targeting CXCL12 from FAP-expressing carcinoma-associated fibroblasts synergizes with anti-PD-L1 immunotherapy in pancreatic cancer. *Proc Natl Acad Sci U S A* 2013;110:20212–7.

48 Smit MJ, Schlecht-Louf G, Neves M, *et al*. The CXCL12/CXCR4/ACKR3 Axis in the Tumor Microenvironment: Signaling, Crosstalk, and Therapeutic Targeting. *Annu Rev Pharmacol Toxicol* 2021;61:541–63.

49 Bolton KL, Chen D, Corona de la Fuente R, *et al*. Molecular Subclasses of Clear Cell Ovarian Carcinoma and Their Impact on Disease Behavior and Outcomes. *Clin Cancer Res* 2022;28:4947–56.

50 Shen J, Ju Z, Zhao W, *et al*. ARID1A deficiency promotes mutability and potentiates therapeutic antitumor immunity unleashed by immune checkpoint blockade. *Nat Med* 2018;24:556–62.

51 Zamarin D, Burger RA, Sill MW, *et al*. Randomized Phase II Trial of Nivolumab Versus Nivolumab and Ipilimumab for Recurrent or Persistent Ovarian Cancer: An NRG Oncology Study. *JCO* 2020;38:1814–23.

52 Gien LT, Enserro DM, Block MS, *et al*. Phase II trial of pembrolizumab and epacadostat in recurrent clear cell carcinoma of the ovary: An NRG oncology study GY016. *Gynecol Oncol* 2024;186:61–8.

53 Liu JF, Herold C, Gray KP, *et al*. Assessment of Combined Nivolumab and Bevacizumab in Relapsed Ovarian Cancer: A Phase 2 Clinical Trial. *JAMA Oncol* 2019;5:1731–8.

54 Zsiros E, Lynam S, Attwood KM, *et al*. Efficacy and Safety of Pembrolizumab in Combination With Bevacizumab and Oral Metronomic Cyclophosphamide in the Treatment of Recurrent Ovarian Cancer: A Phase 2 Nonrandomized Clinical Trial. *JAMA Oncol* 2021;7:78–85.

55 Frentzas S, Austria Mislang AR, Lemech C, *et al*. Phase 1a dose escalation study of ivonescimab (AK112/SMT112), an anti-PD-1/VEGF-A bispecific antibody, in patients with advanced solid tumors. *J Immunother Cancer* 2024;12:e008037.

56 Hamzah J, Jugold M, Kiessling F, *et al*. Vascular normalization in Rgs5-deficient tumours promotes immune destruction. *Nature New Biol* 2008;453:410–4.

57 Martinez-Reyes I, Chandel NS. Cancer metabolism: looking forward. *Nat Rev Cancer* 2021;21:669–80.

58 Trinks A, Milek M, Beule D, *et al*. Robust detection of clinically relevant features in single-cell RNA profiles of patient-matched fresh and formalin-fixed paraffin-embedded (FFPE) lung cancer tissue. *Cell Oncol* 2024;47:1221–31.